Seismo-volcanic sources on Stromboli volcano

Jürgen Neuberg and Richard Luckett
Department of Earth Sciences, University of Leeds, U.K.

Abstract
A detailed analysis of broadband seismic recordings leads to models of eruption mechanisms for Strombolian activity. The data used comprise signals from arrays of nine three-component seismometers and video recordings of visual eruptive activity with precise time reference. As a major tool particle motion analysis is used to locate the seismo-volcanic sources. Here, a surface correction is employed to account for the effects of the steep slopes of the volcanic edifice. After careful filtering of the data single seismic phases can be separated and linked to corresponding eruptive features.

Key words *Stromboli – eruptions – seismic signals*

1. Introduction

In October and November 1992 the University of Leeds in co-operation with the University of Florence deployed nine broadband seismic stations on Stromboli volcano, Italy, in two configurations. The seismic deployment we used in the following study is illustrated in fig. 1. The arrays were in operation for a time period of 5 days in each configuration.

Nine three-component Guralp CMG3 seismometers were used, with a lower corner frequency of 0.03 Hz (30 s period). The upper end of the broadband frequency range at 25 Hz was determined by the sampling rate of 62.5 Hz. The data were recorded by Lennartz MARS88 digital acquisition systems on magneto-optical disks; each station was equipped with a GPS receiver for common time reference. The seismometers were aligned to magnetic north using a compass and declination measurements yielding variations of ±5° were made at each site using a sun compass.

In the period of the deployments Stromboli was in constant activity with eruptive events being seen at the crater area on average once every 5 min. These eruptions occurred at three active vents referred to as crater n. 1, 2, and 3 numbered in a SW to NE direction.

In addition to the seismic broadband arrays the permanent short-period network run by the University of Florence was used, consisting of four 1 Hz vertical component seismometers and one 1 Hz three-component seismometer. The location of the seismometers are depicted in fig. 1. In combination with the seismic measurements a video camera was deployed overlooking the crater area for several hours for both array configurations. Synchronisation with the seismic arrays was achieved by recording a GPS time signal onto the sound track. In this way we can link the visible eruptive activity at the craters with the seismic signals to an accuracy of 0.04 s given by the shutter frequency of the video camera.

With the availability of broadband seismometers, seismology on volcanoes can provide a completely new insight in the dynamics of volcanic eruptions. Even though the long-period part of the seismic spectrum (below 1 Hz) seems to be affected or even dominated by sea microseisms or genuine long-period volcanic tremor, it also contains contributions that
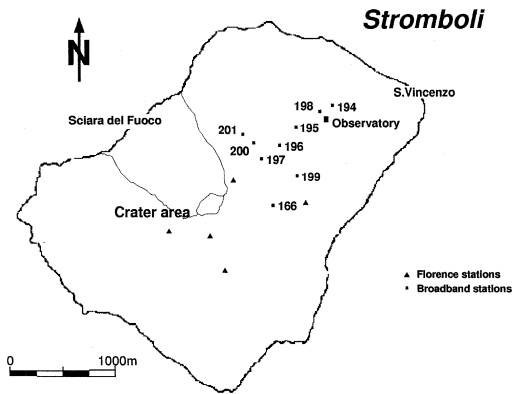
Fig. 1. The numbers shown are the broadband station identifications of the large array, the data of which have been used for this study. The triangles depict the short-period network run by Florence University. A second smaller array was deployed in a diamond-shaped configuration between and including station n. 197 and n. 196.

are essential to the full reconstitution of ground motion due to volcanic shocks. The use of 1 Hz seismometers which have been the conventional tool for seismic monitoring of volcanoes in the past results in the restriction of the high-frequency end of the seismic spectrum and, therefore, to an incomplete reconstruction of the true ground motion. Figure 2a,b presents an example where the broadband displacement seismogram (b) of a seismic event on Stromboli is compared to the displacement of the same event retrieved from a short-period recording (a). The relatively simple wavelet reconstructed from the broadband seismogram is characterised by a short series of step-functions and straight flanks compared to a rather muddled burst of high frequency energy in trace (a). This example stresses the fact that only broadband signals can provide a direct link between observed ground motion and the internal dynamics of the volcanic process causing such
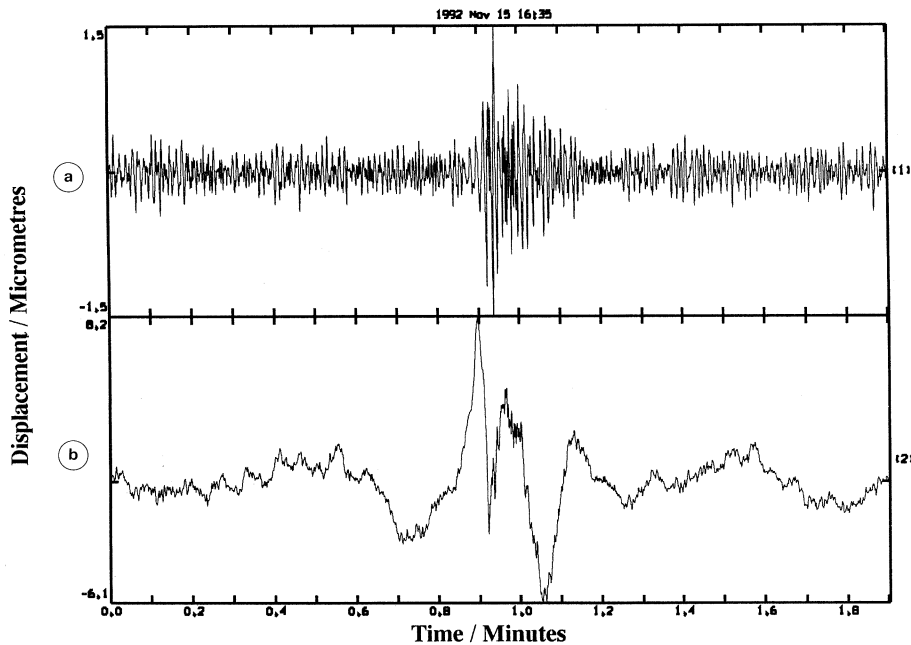
Fig. 2a,b. Comparison between the radial displacements of a short-period recording (a) and a broadband recording (b). The broadband wavelet was reconstituted using a spectral range from 25 Hz to 0.03 Hz (30 s period).

a ground displacement. While the longest period in this example was 30 s, we have used in the following reconstituted displacement seismograms with the spectral content ranging from 25 Hz to 100 s period. Furthermore, standard methods such as particle motion analysis benefit a great deal when applied only to the long-period part of the seismic signal as this is less affected by the often complicated (short-wavelength) stratigraphy of a volcanic edifice.

A summary of the highlights of this seismic experiment is given in Neuberg *et al.* (1994). Here we present (i) an analysis of low-frequency particle motion to determine the location of the seismo-volcanic source and (ii) a detailed study of two eruption-related events and some implications for the eruption mechanism.

2. Source location by particle motion analysis

The location of the seismo-volcanic source on Stromboli is an important first step in its modelling. Of special interest is whether there is one source or more and whether a point source, stationary in time and space, provides an adequate model or whether it is necessary to invoke a more complicated source model. In using particle motion to locate the source an explosive point source is assumed, generating longitudinal waves and excluding the formation of *S*-waves. If an *S*-wave component were present, the particle motion would still be linear but would be the resultant of mutually perpendicular longitudinal and transversal components. Unlike for a *P*-wave the direction of particle motion would not point to the source. However, if a constant ratio between both wavetypes is assumed then the particle motion would still indicate whether there is one stationary source or not.

2.1. *Method*

If a seismic wave has a distinct particle motion it is possible to use a three-component recording to reveal its direction of propagation.

The method used here is described in Jurkevics (1988). Time slots of 20 s containing a seismo-volcanic event were extracted from one-hour time windows of band-pass filtered data. The covariance matrix was then calculated by finding the variances for each combination of the three components. The eigenvalues and eigenvectors were determined for this matrix representing the principal axes of the polarisation ellipse. From these vectors the values for the azimuth and the angle of incidence were calculated. The three eigenvalues λ_i were ordered by magnitude such that $\lambda_1 > \lambda_2 > \lambda_3$, and the relative magnitudes used to obtain a measure of rectilinearity R defined as

$$R = 1 - (\lambda_2 + \lambda_3)/2\lambda_1.$$

In the case of a longitudinal particle motion along a straight line, $\lambda_1 \gg \lambda_2, \lambda_3$, the rectilinearity $R \cong 1$.

Just over 200 events were investigated in this way for three narrow frequency bands: 0.04-0.08 Hz, 0.14-0.18 Hz, and 0.34-0.38 Hz. These lower frequencies were chosen because particle motion with high linearity can be found for frequencies below 0.5 Hz suggesting that the particle motion corresponds to that of a *P*-wave rather than a combination of surface waves and all sorts of scattered waves dominating the higher frequency range (Neuberg *et al.*, 1994).

The crater area is approximately 2 km from the furthest station and for longitudinal wave velocities the wavelengths corresponding to these low frequencies are much longer than this. Figure 3a-c shows the particle motion for the event in fig. 2a,b bandpass filtered between 0.04 and 0.08 Hz together with particle motions at higher frequencies for comparison. For the lower frequency range a longitudinal wave emerging directly from the source is postulated.

2.2. *Surface correction*

A longitudinal wave reflected at a free surface undergoes partial conversion to a vertically polarised shear wave. This makes the to-
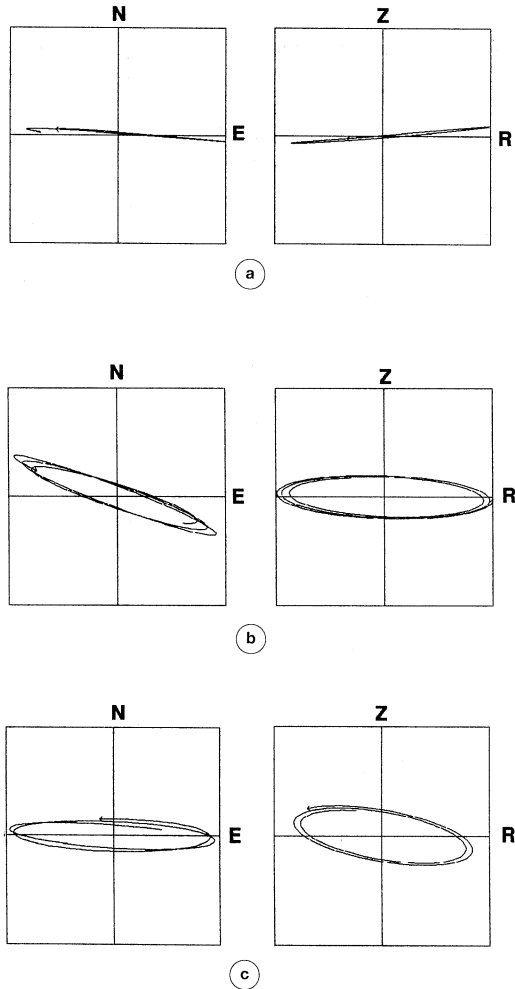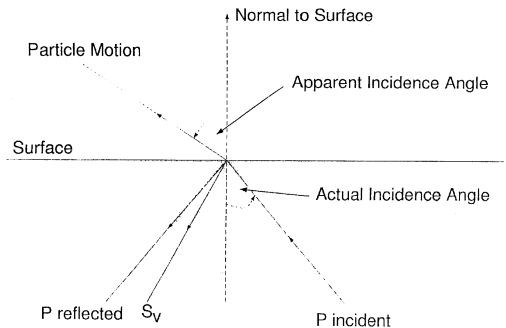
Fig. 3a,c. Particle motion for the event in fig. 1 bandpass filtered for three different frequency bands: a) 0.04-0.08 Hz; b) 0.54-0.58 Hz; c) 0.86-0.90 Hz. Note the nearly linear motion for the lowest frequency range and the concentration of energy in the horizontal plane for all frequency bands.

the V_P/V_S ratio. The boundary conditions for the displacement at the free surface then provide the link to the true angle of incidence pointing to the seismic source. Here we used a formulation given by Jepsen and Kennett (1990). Once the real angle of incidence (to the free surface) is determined the projection onto the coordinate axes provides the true azimuth and the angle to the vertical in direction to the source. For the long wavelengths investigated here it was necessary to average the slope of the volcano between the summit and the sea passing through each seismic station.

The method used to obtain the surface correction assumes that the incident wave includes no shear components and is a plane wave. This would be the case in the far-field. In our investigation the stations are less than one wavelength from the source and therefore located in the near-field. That has two implications: the waves are spherical rather than plane, and a time-dependent source term is included in the mathematical representation of the displacement. While the first implication clearly does not affect the angles under consideration, we have to assume that the near-field term which still describes a longitudinal perturbation satisfies the same boundary conditions as the displacement of a purely elastic wave. The resulting reflection angles would thus be the same

tal wavefield at the surface more complex (see fig. 4) due to the superposition of incident, reflected and converted waves. In order to retrieve the true direction of the incident wave it is necessary to determine the apparent angle of incidence for a given surface normal vector (averaged over the size of a Fresnel zone) and

Fig. 4. Partial conversion of a longitudinal wave at a free surface into a vertically polarised shear wave. The wavefield measured at the free surface is a superposition of the three phases.

allowing the same formulation to be used for both parts of the wavefield, the near-field term and the far-field term.

2.3. *Results of particle motion analysis*

The results of the particle motion analysis are summarized in table I. Striking is that there is so little scatter in the true azimuth and angle of incidence at each station despite the fact that data from all three vents were used indiscriminately. Note that the standard deviation at the seismic station nearest to the craters (n. 166) is only ± 4 degrees whereas the outermost craters subtend an angle of 10 degrees at that station. This clearly indicates a common seismic source for events associated with different craters.

Table I. Angles found by solving the eigenvalue problem for the covariance matrices of the three components at each seismic station. 207 events from all craters were averaged. Bandpass filtering was carried out over a two hour window and the particle motion calculated for a 20 s window. The stations are given in order of decreasing altitude.

	Declination corrected azimuths for 207 band passed events/degrees					
	0.04 to 0.08 Hz		0.14 to 0.18 Hz		0.34 to 0.38 Hz	
	Mean	S.D.	Mean	S.D.	Mean	S.D.
197	88	12	91	32	89	19
200	82	12	86	38	83	21
166	114	4	111	30	111	20
199	93	20	91	33	90	22
201	90	15	92	36	89	21
196	90	12	91	37	87	24
195	89	14	88	42	84	30
198	66	28	96	51	81	41
194	64	34	88	44	83	45

	Angles to vertical for 207 band passed events/degrees					
	0.04 to 0.08 Hz		0.14 to 0.18 Hz		0.34 to 0.38 Hz	
	Mean	S.D.	Mean	S.D.	Mean	S.D.
197	94	3	95	15	95	12
200	96	4	92	14	98	12
166	90	3	91	14	91	12
199	89	4	88	16	85	14
201	97	6	92	18	97	15
196	93	4	90	18	90	16
195	92	7	87	19	87	18
198	92	5	87	24	84	27
194	91	5	90	2	90	1

Another interesting feature is the difference in scatter between the frequency bands. One would expect the scatter to increase as the centre frequency increases and phases with decreasing rectilinearity such as scattered and surface waves become more dominant. This is generally the case with the exception of a frequency band centered on 0.16 Hz which has a larger standard deviation than in the case of higher frequencies. This is because the main spectral peak due to sea microseisms is located in this band providing a strong noise source with respect to the seismo-volcanic events.

The surface corrections found for the mean values for the lowest frequency range are shown in table II. The largest difference in azimuth is merely 5 degrees whereas the angle of incidence is corrected by 10 to 16 degrees. Tracing back the particle motions suggests a seismic source as indicated in fig. 5. The vectors do not meet up as well as might be expected from the small scatter at each station (table I). One reason for this may be that using a time window of 20 s an averaging over several different seismic phases is made. If these
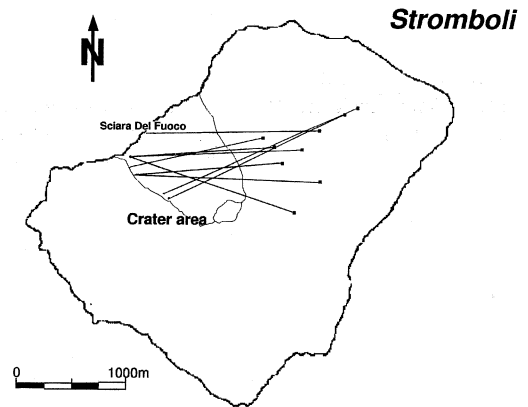
Fig. 5. Directions of particle motion in the horizontal plane plotted onto a map for the frequency range 0.04-0.08 Hz. The azimuths have been corrected both for declination and for surface effects.

different phases came from slightly different directions the averaging process would affect the result at different stations differently. In the following section we explore (rather speculatively) such an eruption scenario.

Table II. The effect on the average azimuth and angle to vertical after applying the surface correction.

Mean values for 207 band passed events 0.04 to 0.08 Hz				
	Azimuth/degrees		Angle to vertical/degrees	
	Before surface correction	After surface correction	Before surface correction	After surface correction
197	88	86	86	73
200	82	78	84	72
166	114	109	90	75
199	93	92	91	75
201	90	86	83	69
196	90	88	87	75
195	89	88	89	79
198	66	66	88	75
194	64	64	90	79

3. Detailed study of two eruption-related events

The three different craters on Stromboli exhibited three distinct types of eruptive activity, and correspondingly three different types of seismic signatures. Figure 6 shows displacement seismograms for the three craters in all seismic components. Crater n. 1 was a rather widely spraying lava source, the eruptions from which were accompanied by a dark ash cloud sometimes evolving in a plume. The corresponding seismic signal (fig. 6) is characterised by a W-like wavelet the first part of which always precedes the onset of the visible eruption. The existence of such an ash plume at this crater indicates magma components that have been cooled prior to ejection (Wilson,

personal communication). The second crater produces gas jets that last for 15-20 s and are accompanied by relatively little ejecta in the first phase of the eruption. The seismic signature is a wide-stretched trough which has a small amplitude and would not be detected in the short-period recording at all. Due to the poor signal-to-noise ratio, we do not consider that vent any further in this study. Crater n. 3 displayed sharp lava fountains that reached 150-200 m height and lasted only a few seconds. The corresponding seismic signal presents a V-like wavelet that is preceded and superimposed by an oscillation with a period ranging from 1-2 s.

In the following we focus on crater n. 1 and n. 3 and analyse in detail the course of two seismo-volcanic events by incorporating the in-
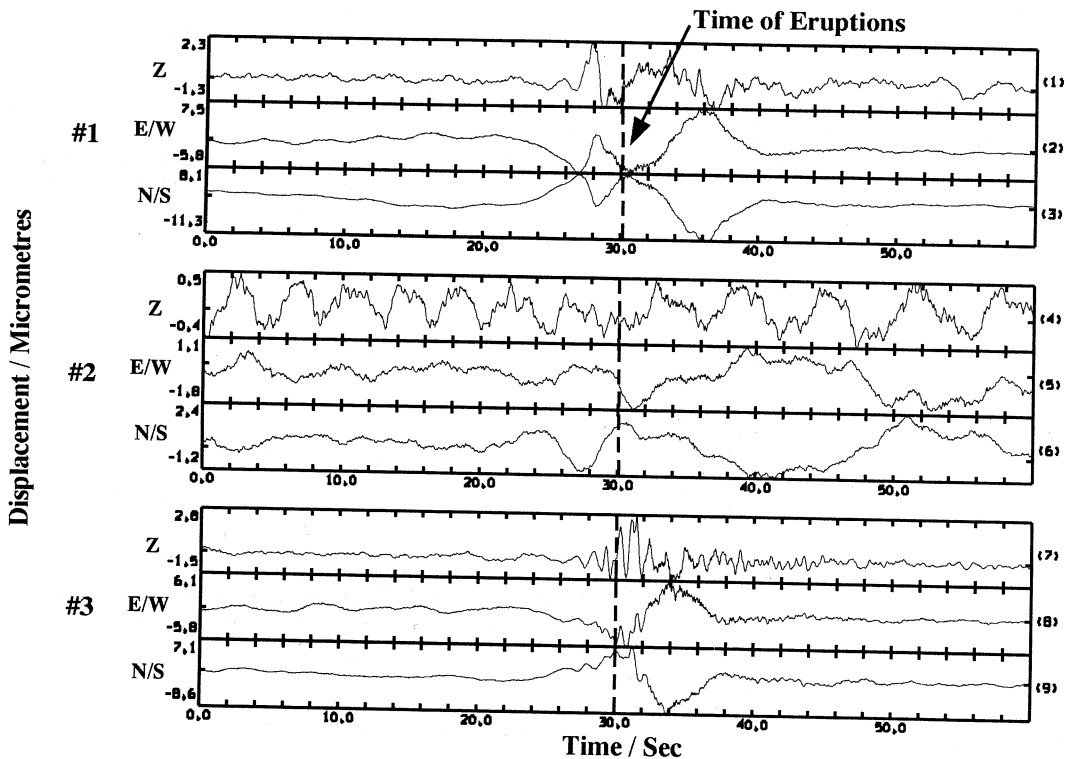

Fig. 6. Vertical, E/W and N/S component of the displacement for three different eruption-related events recorded at station n. 166. Each crater produces a different characteristic seismic signature.

formation from the video recording. We employ various filter techniques to separate and enhance certain seismic features, and use particle motion analysis as described above to trace back the origin of the ground motion. On the basis of this analysis we speculate about possible source mechanisms for both craters.

Crater n. 1 – The vertical, radial and transversal components of displacement of a seismo-volcanic event related to crater n. 1 and recorded at station 166 (fig. 1) are shown in fig. 7. The amplitudes have been normalised to give an indication of the energy partition into single components. The onset of the visible

eruption, *i.e.* the frame of the video recording that showed the first ejecta, is marked as well as the end of the eruption. In addition these points in time have been delayed by the travel time of a *P*-wave assuming a *P*-wave velocity of 1200 m/s and a distance between crater and seismic station of 1100 m. This indicates the time when a perturbation in the displacement that has been caused in the crater area would arrive at the seismic station.

Furthermore, the onset of a high-frequency phase caused by the arrival of the ground-coupled air wave (Braun and Ripepe, 1993) is depicted together with the time when this air wave has been produced in the crater area. We
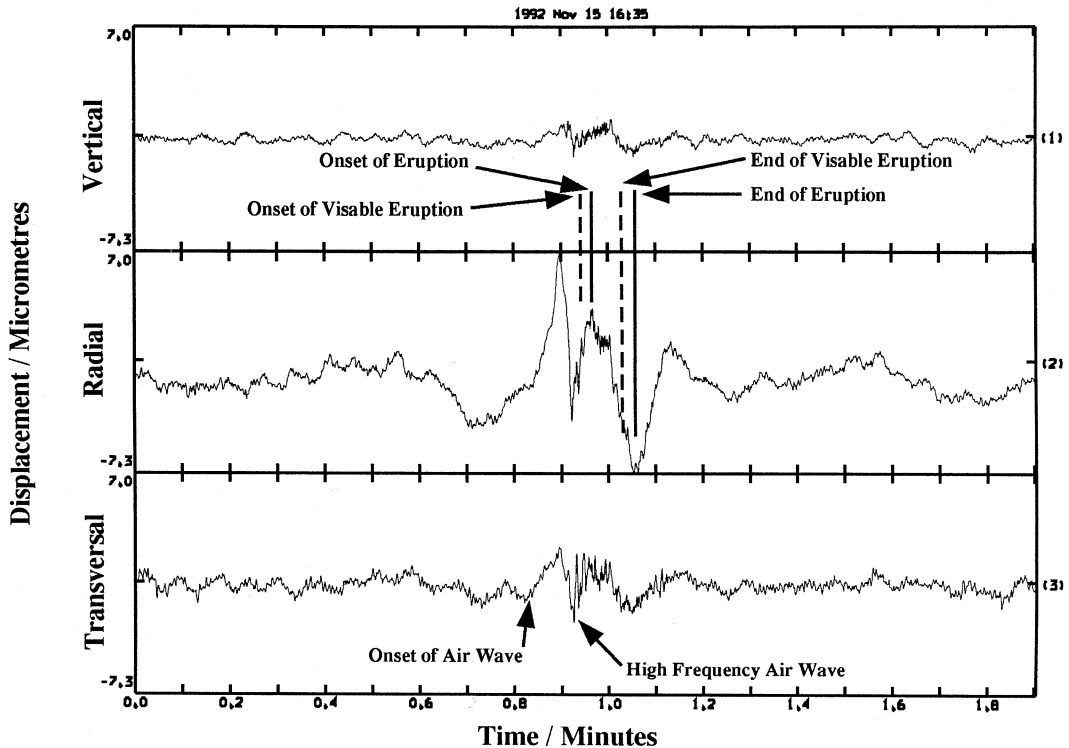
Fig. 7. Three displacement components of an event related to crater n. 1 and recorded at station 166. The normalised amplitudes indicate the energy partition between the components. The radial component is dominated by a ground motion towards the source in two steps: a «trigger» and an «eruptive phase». The duration of the visible eruption as recorded by the video and delayed with the *P*-wave velocity is indicated as well as the arrival of the high-frequent air wave.
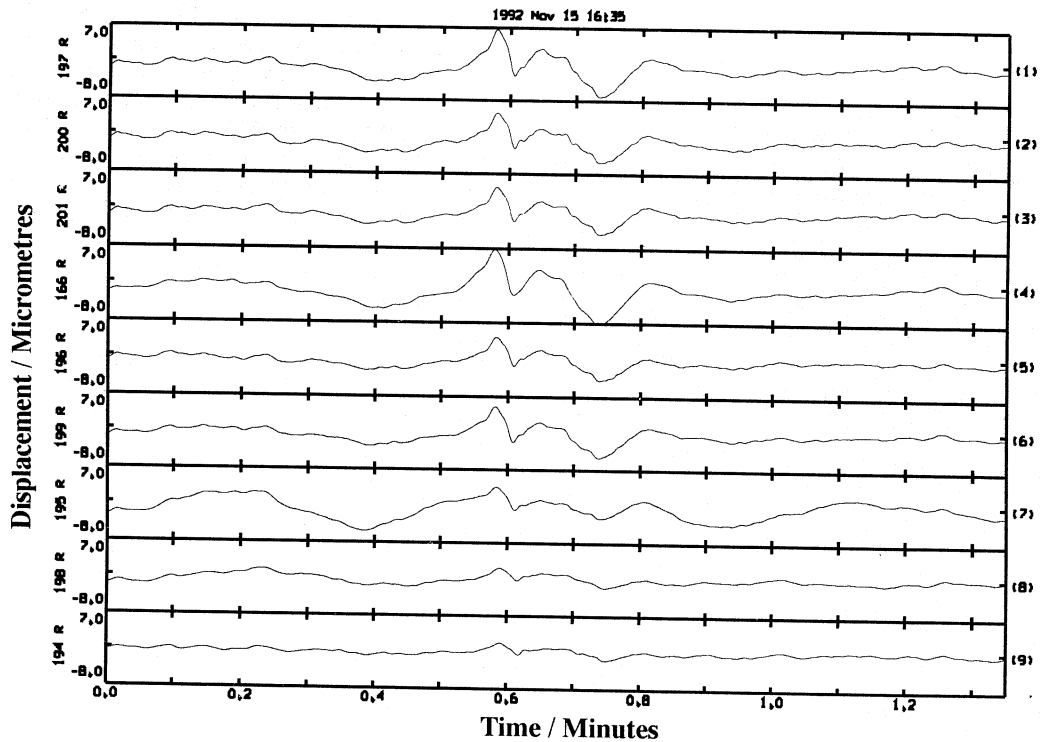
Fig. 8. Low-pass filtered radial displacements in the order of increasing distance from the crater area. All seismic stations record a coherent signal.

assume again a distance of 1100 m to the crater and in the case of an air wave a propagation velocity of 340 m/s.

Most of the ground motion takes place in the radial direction where the negative sign indicates a contracting source and the positive sign an expanding source. The event is initiated by a steadily increasing dilatation followed by a sudden contraction. After a relaxation to an undisturbed level an even larger contraction follows which coincides in time with both the onset and the duration of the eruption.

After the application of a low-pass filter with a cut-off frequency of 2 Hz the radial components of all nine stations are shown in fig. 8 in order of increasing distance from the crater area. All stations exhibit a similar displacement, at least in the limits of the azimuthal coverage of 55 degrees. We now sepa-

rate the two parts of the W-wavelet – the initial contraction and the part coinciding with the eruption – and determine by cross-correlation the differential travel time for each part at all stations. By using the low-pass filtered horizontal components of the displacement the particle motion of the two parts are determined. Figure 9 summarises the results where the length of the particle motion vectors represent the differential travel time: each part of the wavelet has a separate source location. We refer in the following to the first part of the wavelet as the «trigger-event» and to the second as the «eruptive flow».

On the basis of these observations we speculate about the following eruption process for crater n. 1:

i) a degassing process causes a pressure build-up and an inflation of a section of the

385
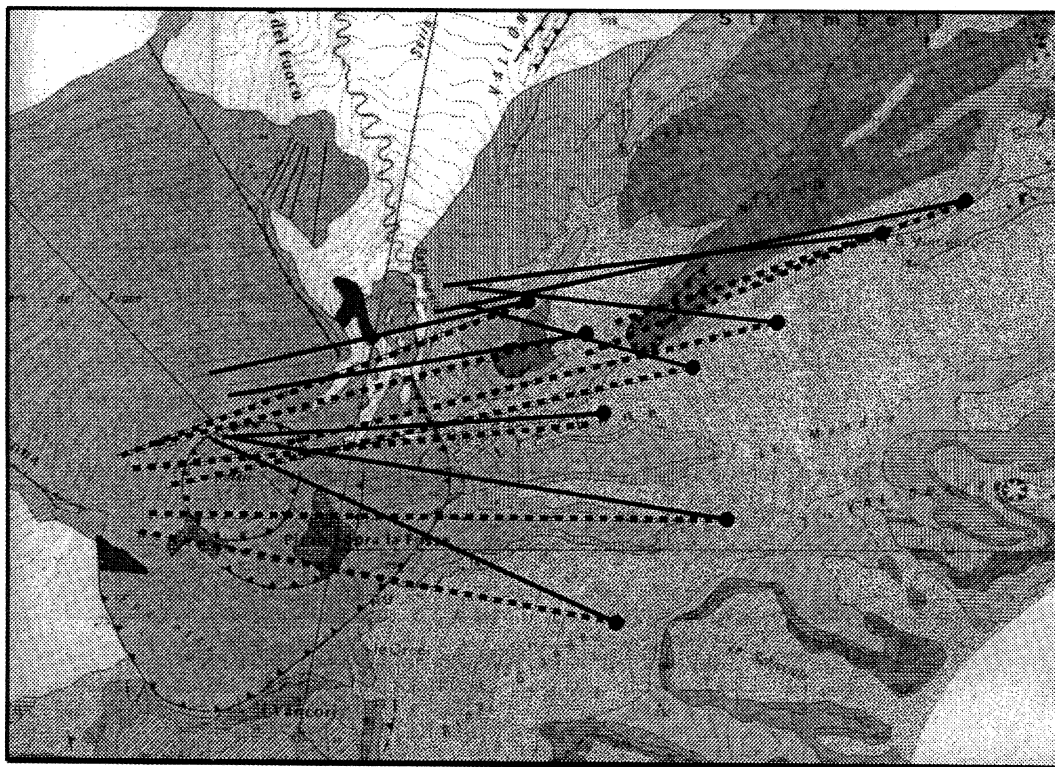
Fig. 9. Particle motion of the «trigger phase» (solid line) and «eruptive phase» (dotted line) for an eruption at crater n. 1. The length of the particle motion vectors corresponds to the differential travel time projected onto the horizontal plane. Both phases seem to have different source locations. (Map by Keller *et al.*, 1993.)

conduit system. This is detected as a ground motion away from the source. The yield strength of the magma causing the pressure build-up could be the result of either differential cooling in the upper part of the conduit system of crater n. 1 or simply the slowing down of the magma flow. Adopting the model of a non-Newtonian fluid both processes would result in an increase of viscosity and a corresponding increase of the yield strength (Parfitt and Wilson, 1994). The ash cloud at crater n. 1 is an indicator for partially cooled material;

ii) when the pressure has built up to exceed the yield strength of the magma, fluid flow is set off and magma is pushed through dikes. According to Bernoulli's equation this leads to a pressure drop which is seen as a contracting ground motion (towards the source) at the seismic stations;

iii) this initial pressure drop triggers an accelerated degassing process which finally leads to the actual eruption and the accompanying seismic flow-signature with a ground motion towards the crater area for the duration of the eruption. The process ends its cycle with relaxation.

Figure 10 depicts several seismo-volcanic events related to crater n. 1 recorded at station 166. A comparison between different events shows that certain features of the seismic signature vary significantly: the time lag between «trigger-event» and «eruptive flow», as well as the period between the onset of the «eruptive flow» and the visible eruption. This could indi-
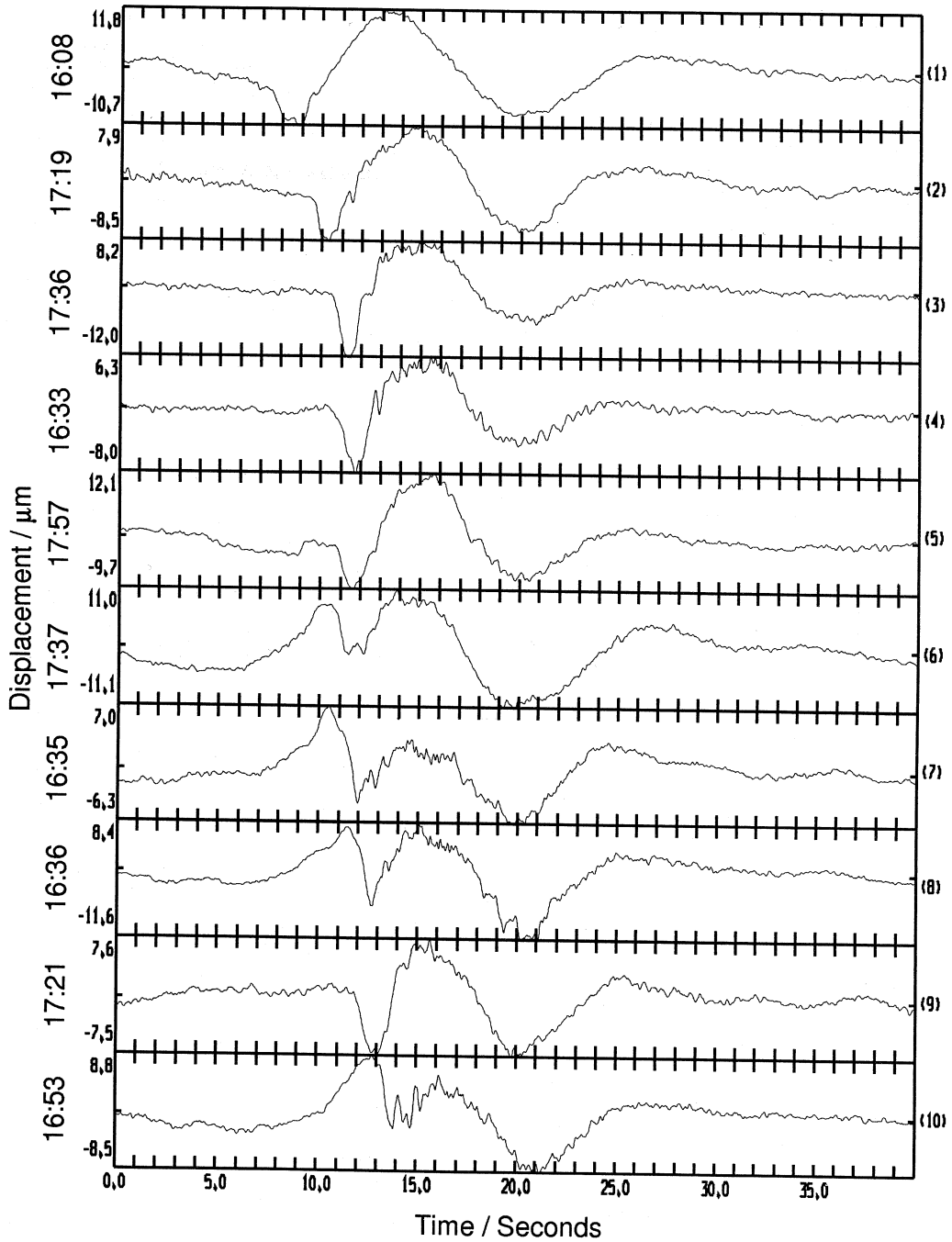
Fig. 10. Different examples of events related to crater n. 1 and recorded at station n. 166. The time difference between the «trigger» and «eruptive phase» varies significantly from event to event.

387

cate that the triggering pressure drop takes place at different depths and with various magnitudes leading to fast or delayed eruptive responses. A proper quantification of such a source mechanism can only be achieved by fluid dynamic modelling.

Crater n. 3 – The wavelets related to seismo-volcanic events from crater n. 3 consist of a 1-2 s oscillation superimposed by a later V-shaped phase. The application of a 2 Hz low-pass filter to get rid of the surface wave noise and a subsequent band-pass filter with corner frequencies at 0.5 Hz and 1 Hz provided the separation between oscillation and V-wavelet. Furthermore, the analysis of particle motion of the oscillation revealed a second phase roughly perpendicular to the first seismic arrival. Figure 11 summarises the different seismic phases involved; the examples have been recorded at 166. The seismic phases are referred to as «oscillation» and «eruptive flow» suggesting that the V-shaped waveform, the particle motion of which points again towards the source, is caused by magma flow leading to the eruptive lava fountain. The relevant times taken from the video recording corresponding to those in fig. 7 for crater n. 1 are also shown in fig. 11.

The striking feature here is the pronounced difference in the direction of particle motion between «oscillation» and «eruptive flow» as
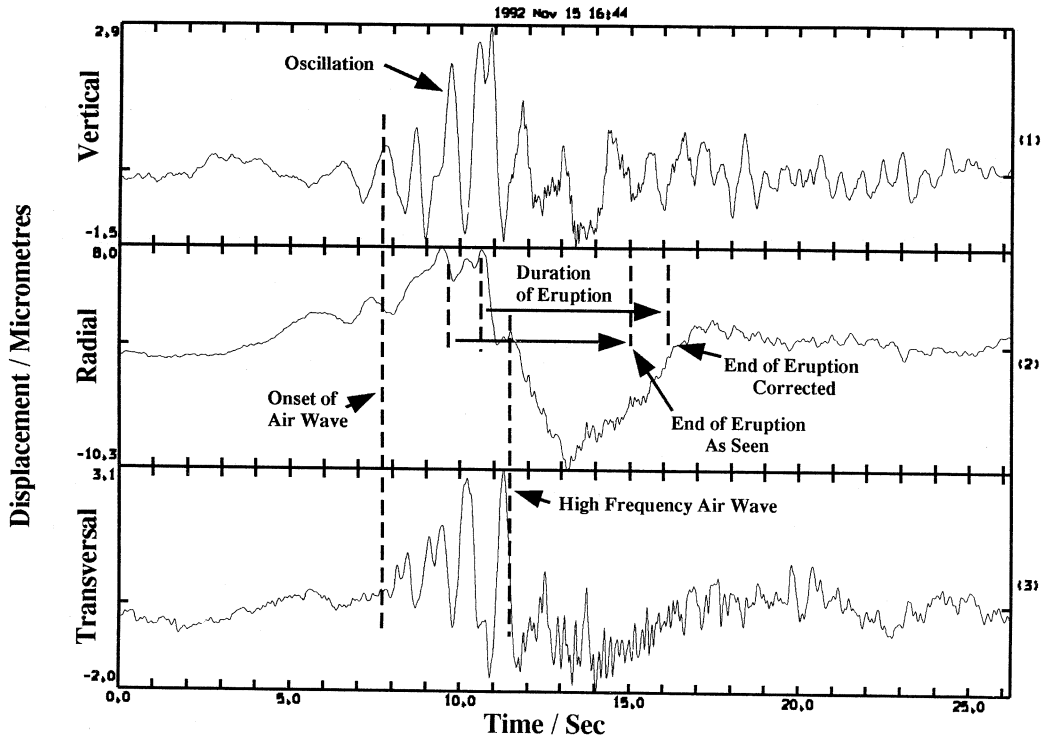
Fig. 11. Three displacement components of an event related to crater n. 3 and recorded at station n. 166. Note the different scales for all components. The radial component is dominated by a ground motion towards the source while the smaller vertical and transversal components show a preceding oscillation. The duration of the visible eruption as recorded by the video and delayed with the *P*-wave velocity is indicated as well as the arrival of the high-frequent air wave.
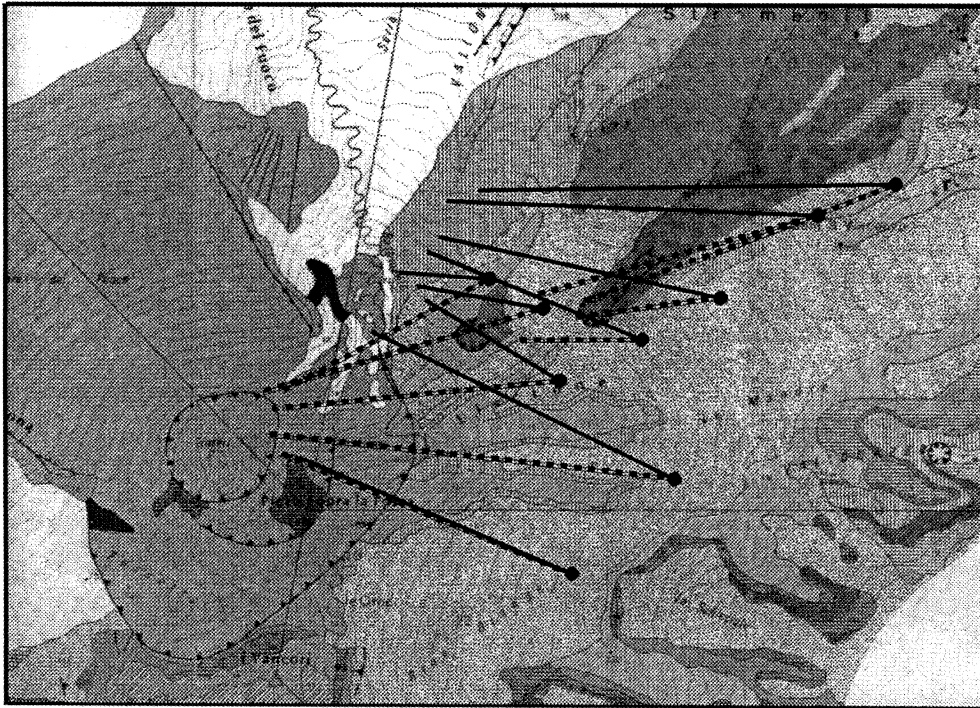
Fig. 12. Particle motion of the «trigger phase» (solid line) and «eruptive phase» (dotted line) for an eruption at crater n. 3. The length of the particle motion vectors corresponds to the differential travel time projected onto the horizontal plane. While the particle motions related to the triggering oscillation cover a wide area, the particle motion of the eruptive phase converges near the crater area.

demonstrated in fig. 12. In fact, the particle motion vectors of the oscillation do not converge to a point source but designate a linear source area with a number of clusters. These coincide with the occurrence of magmatic dikes and a previous centre of eruptive activity (Keller *et al.*, 1993). The flow-related parts of the seismic signature point quite clearly to the crater area.

A speculative interpretation based on these observations lead to the following source process for crater n. 3:

i) magma flow in a feeding dike system outlined as the source area of the «oscillation» in fig. 8 leads to a resonance effect sustaining a narrow band pressure fluctuation with 1-2 s period. Those oscillations have been observed and modelled by Chouet (1988) as a resonating fluid-filled crack;

ii) as the amplitude of such a resonating oscillation increases, a decompressional phase exceeds the degassing threshold and leads to a short but – due to the narrow vent – explosive eruption. The corresponding fluid flow generates again a pressure drop for exactly the duration of the eruption. The cycle ends with the relaxation to ambient pressure and zero displacement.

Continuous activity at crater n. 3 – The video recordings of activity at crater n. 3 between pronounced seismo-volcanic events shows a weak but on-going eruptive activity. This is also reflected by significant spectral

peaks in the seismic background noise with dominant frequencies around 1 Hz. Assuming an open vent, in contrast to crater n. 1, the ongoing activity can be interpreted as a continuous degassing process where the dominant frequencies as seen in the seismic spectrum are controlled by the geometry of the conduit which acts as a resonator. The pulse-like excitation of such a system could be driven by a series of small explosions fed by continuous degassing and triggered by an excessive pressure in the forming bubbles (Blackburn et al., 1976).

In order to produce a peaked spectrum, the series of exploding gas bubbles does not necessarily need to be periodic as long as the (ran-dom) excitation mechanism drives a resonant system. This is demonstrated in fig. 13a-c where a short wavetrain represents the resonance behaviour in the conduit or vent. This wavetrain with a dominant frequency of 1 Hz is repeated by convolving it with a series of randomly distributed spikes. Figure 13c shows the amplitude spectrum of the resulting time series, which exhibits many spliced spectral lines grouped around the original resonance frequency. This type of spectral peak is often observed in contrast to very sharp spectral lines caused by harmonic volcanic tremor, and can be explained by a series of small explosions.
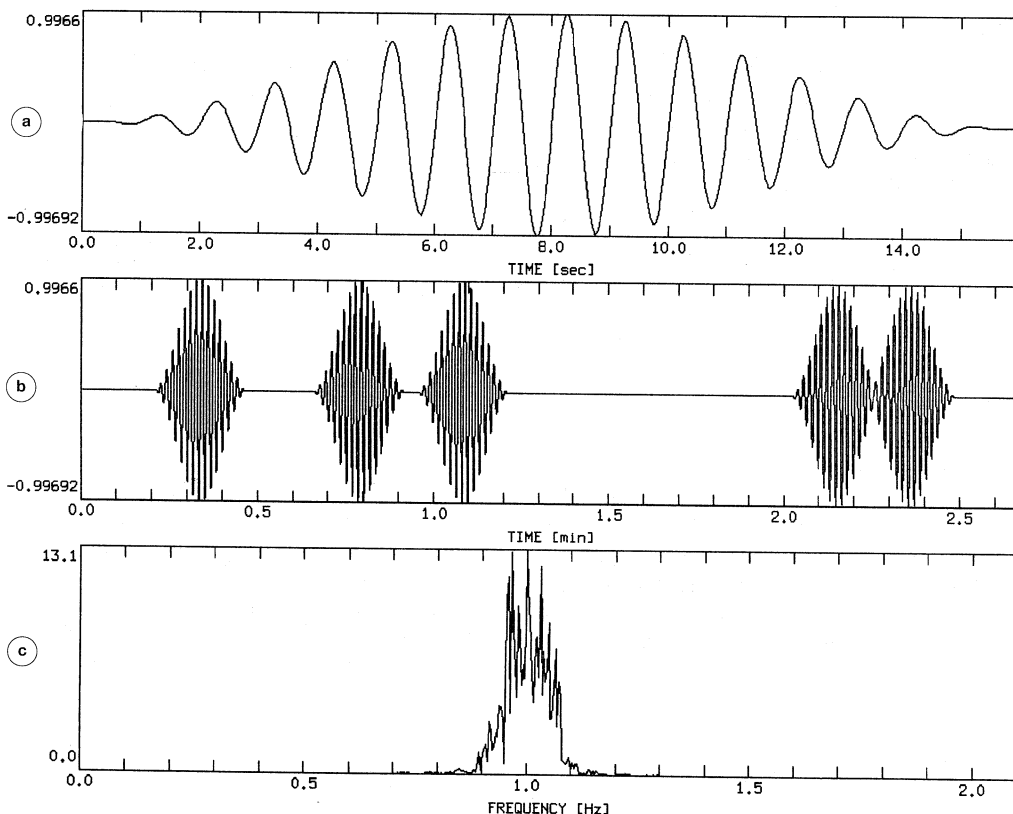
Fig. 13a-c. A synthetic 1 Hz wavetrain (a) is convolved with randomly distributed pulses to create a time series (b) with repeating resonating wavelets. The corresponding spectrum (c) shows a group of spliced spectral lines centred at 1 Hz.

4. Discussion and conclusions

The careful analysis of seismic broadband signals, in connection with a video recording of visible eruptive activity, allowed us to speculate about different source mechanisms for eruption-related events at two craters on Stromboli. The most striking feature is that the fluid flow during an eruption can be linked to a ground motion towards the seismic source, hence, indicating a contracting source mechanism as modelled by Bernoulli's equation. We distinguished for both craters between a preceding trigger mechanism and the actual eruption. By looking at a large number of events it was found that for the eruptive phase all sources lie in the same area regardless of the active vent. For crater n. 1 this trigger was represented by a smaller fluid flow that we interpreted as the loosening of a slug or section of material with a higher viscosity and yield strength, leading to an accelerated degassing. For crater n. 3 this trigger was provided by a resonating oscillation of magma in an extended dike system. The duration of the subsequent eruptive phases in the seismic signals can be clearly associated with the times of onset and end of the visible eruption.

The location of the seismo-volcanic source is mainly based on the analysis of particle motion and, therefore, highly dependent on the seismic source model. We exclusively employed a compressional/dilatational source that produces only P-waves, but no S-waves. If shear stress was involved in the source mechanism the resulting particle motion in the near-field of the source would be a superposition of P- and S-waves and the direction of particle motion would not point to the seismic source. Consequently, all source locations mentioned in this study would be affected. An exact determination of the radiation pattern of the seismo-volcanic source can only be achieved by deploying several broadband stations close to the summit area with a full azimuthal coverage.

We conclude that eruptions on Stromboli take place in (i) a continuous manner where a series of small explosions at crater n. 3 are responsible for a peaked background spectrum, usually referred to as volcanic tremor; (ii) due to a triggering oscillation of magma in a dike system connected to an open vent at crater n. 3; and (iii) at crater n. 1 where the trigger mechanism can be associated with the opening of the vent with a subsequent pressure drop that leads to an accelerated degassing. Fluid dynamic modelling will have to be used to quantify these models and prove their feasibility.

REFERENCES

BLACKBURN, E.A., L. WILSON and R.S.J. SPARKS (1976): Mechanisms and dynamics of Strombolian activity, *J. Geol. Soc. Lond.*, **132**, 429-440.

BRAUN, T. and M. RIPEPE (1993): Interaction of seismic and air waves recorded on Stromboli volcano, *Geophys. Res. Lett.*, **20**, 65-68.

CHOUET, B. (1988): Resonance of a fluid-driven crack: Radiation properties and implications for the source of long-period events and harmonic tremor, *J. Geophys. Res.*, **93**, 4375-4400.

JEPSEN, D.C. and B.L.N. KENNETT (1990): Three component analysis of regional seismograms, *Bull. Seism. Soc. Am.*, **80**, 2032-2052.

JURKEVICS, A. (1988): Polarisation analysis of three-component array data, *Bull. Seism. Soc. Am.*, **78**, 1725-1743.

KELLER, J., I. HORNIG-KJARSGAARD, U. KOBERSKI, E. STADLBAUER and R. LENHART (1993): Geological Map of the island of Stromboli – scale 1:10000, *Acta Vulcanol.*, vol. 3 (Appendix).

NEUBERG, J., R. LUCKETT, M. RIPEPE and T. BRAUN (1994): Highlights from a seismic broadband array on Stromboli volcano, *Geophys. Res. Lett.*, **21** (9), 749-752.

PARFITT, E.A. and L. WILSON (1994): The 1983-86 Pu'u 'O'o eruption of Kilauea volcano, Hawaii: a study of dike geometry and eruption mechanisms for a long-lived eruption, *J. Volcanol. Geotherm. Res.*, **59**, 179-205.